Detection and Visualization of Splat and Antisplat Events in Turbulent Flows

Baldwin Nsonga, Martin Niemann, Jochen Fröhlich, Joachim Staib,
Stefan Gumhold, and Gerik Scheuermann, *Member, IEEE*

Abstract—Splat and antisplat events are a widely found phenomenon in three-dimensional turbulent flow fields. Splats are observed when fluid locally impinges on an impermeable surface transferring energy from the normal component to the tangential velocity components, while antisplats relate to the inverted situation. These events affect a variety of flow properties, such as the transfer of kinetic energy between velocity components and the transfer of heat, so that their investigation can provide new insight into these issues. Here, we propose the first Lagrangian method for the detection of splats and antisplats as features of an unsteady flow field. Our method utilizes the concept of strain tensors on flow-embedded flat surfaces to extract disjoint regions in which splat and antisplat events of arbitrary scale occur. We validate the method with artificial flow fields of increasing complexity. Subsequently, the method is used to analyze application data stemming from a direct numerical simulation of the turbulent flow over a backward facing step. Our results show that splat and antisplat events can be identified efficiently and reliably even in such a complex situation, demonstrating that the new method constitutes a well-suited tool for the analysis of turbulent flows.

Index Terms—Flow visualization, visualization techniques and methodologies

✦

1 INTRODUCTION

THE visualization of turbulent flow fields poses a major challenge in the field of scientific visualization. With increasing computational power turbulence-resolving simulations on finer and finer grids can be conducted providing an enormous wealth of data with increasing size and resolution allowing a detailed examination of the flow. Especially the dynamics of near-wall flows are of interest, as it has a significant impact on properties relevant to various applications, such as flow resistance, heat transfer, transfer of mass, solidification, etc. However, scientific knowledge has to be extracted from these data sets dramatically increasing in size and resolution. One successful approach in the visual analysis of flow fields is to employ feature-based methods. A variety of features have been introduced in the literature, allowing for a purposive investigation of the emergence, development, and interaction of specific features, e.g., vortices. Yet, the interaction of turbulent flows with boundary structures can only be partially examined with existing features. The turbulent boundary layer at solid walls and the features therein have been widely investigated. However, less prominent cases like shear-free boundaries feature different common phenomena. Splat and antisplat events are common on this type of boundary but also occur on solid walls in regions with negligible mean shear, for instance in the reattachment region behind a sudden change of cross section as investigated in the present paper. These events have been subject to fluid dynamics research for more than two decades [1]. However, at present no direct method exists for their reliable detection and visualization.

Splats are defined as regions wherein a turbulent flow bulk fluid locally and instantaneously impinges on an impermeable boundary [2]. They transfer energy from the normal velocity component to the tangential components. An antisplat is the reversed phenomenon, transferring energy from the tangential component to the normal component, injecting it into the bulk flow. Splats have been found to influence a variety of flow properties in the flow near solid walls [3], i.e., stresses on boundaries [4], vortices [5], [6], and heat transfer [7]. In addition, they are dominant structures at free surfaces [8]. Indicators for splats and antisplats discussed in the fluid dynamics literature are often found to be a result of the presence or interaction of these phenomena. These indicators have an instantaneous scope whereby splats and antisplats are dynamic phenomena. Furthermore, the only current definition provided in fluid dynamic literature is fuzzy.

This paper results from a collaboration of visualization experts (BN, JS, SG, GS) with domain experts in fluid mechanics (MN, JF). The goal is to develop a method for the extraction of splats and antisplats from given highly resolved direct numerical simulations of the unsteady

• B. Nsonga and G. Scheuermann are with the Institute of Computer Science, Leipzig University, Augustusplatz 10, Leipzig 04109, Germany.
E-mail: {nsonga, scheuermann}@informatik.uni-leipzig.de.
• J. Staib and S. Gumhold are with the Institute of Software and Multimedia Technology, TU Dresden, Nöthnitzer Straße 46, Dresden 01187, Germany.
E-mail: {joachim.staib, stefan.gumhold}@tu-dresden.de.
• M. Niemann and J. Fröhlich are with the Institute of Fluid Mechanics, TU Dresden, George-Bähr-Straße-3c, Dresden 01062, Germany.
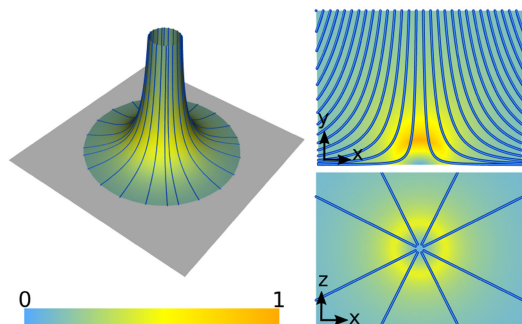E-mail: {martin.niemann, jochen.froehlich}@tu-dresden.de.

Fig. 1. Stagnation flow pattern. This image illustrates a stagnation flow in which the flow moving in the negative y-direction impinges a boundary aligned with the x-z plane. The top left image shows an exemplary stream surface in the three dimensional domain with streamlines (blue). A side and top view of the flow pattern in shown in the right images respectively. The coloring of the stream surface and the cross sections is the mapping of the velocity magnitude in the velocity field.

turbulent flow field. After a brief introduction to the physical nature of splats and antisplats, we introduce a clear, objective definition of a splat/antisplat as a feature in three-dimensional space. Second, and related to this, we present the first Lagrangian method for the extraction of these features. Together with that, we provide a specialized visualization approach for the boundary surface with the main focus on the strength of a splat/antisplat event. It is completed by a three-dimensional visualization technique for these events with an emphasis on structural and spatial perception. The new method is validated utilizing artificial flow fields of increasing complexity. We then apply our technique to a full-scale application case, direct numerical simulation data of the turbulent flow over a backward-facing step (BFS). This flow configuration is found to produce splat and antisplat events in the recirculation and reattachment area at the wall behind the step. Our numerical experiments demonstrate that the proposed method reliably detects these events in turbulent flows and that the developed tool is ready for practical applications by researchers in fluid mechanics.

2   SPLATS AND ANTISPLATS

2.1   State of the art

First introduced by Bradshaw [9] when investigating the pressure Poisson equation in turbulent flow, splats (also referred to as *upwelling*, *upsurge* or *updraught* in the context of free-surface flows) have been found to be an important feature of turbulent flows [8]. They occur especially in shear-free flows like open channels which feature a free surface at the top of the domain prohibiting normal flow but allowing tangential velocity components. Perot and Moin [1] defined a splat event as a local region of stagnation of flow resulting from fluid impinging on a wall. Because fluid cannot penetrate the boundary, any fluid element moving towards the wall must change direction and, subsequently, orient parallel to the wall. By this mechanism, a splat event transfers energy from the wall-normal velocity component to the two tangential velocity components, increasing the tangential turbulent stresses near the wall. Perot and Moin investigated splats in shear-free boundary layers and then extended their study by

considering viscous effects at solid walls. They also define the opposite event to splats, antisplats, which occur when fluid elements moving tangentially to the wall detach and are transported in wall-normal direction. Focusing on the effects of splat events on the Reynolds stress budgets, they deduced that the imbalance of splats and antisplats results in an energy transfer between Reynolds stress components. This imbalance was further investigated by Bodart et al. [10].

Splats were also observed in experiments and simulations of open channel flow [8], [11], [12]. Here, the interaction of splats and antisplats was observed to result in vortices rotating tangentially to the free surface [13]. These vortices are involved in the formation of hairpin vortices and are responsible for the increase of wall parallel stresses [6]. Dejoan et al. [14] observed similar phenomena in a wall jet.

More complex cases arise when the cross-section of the flow varies. Splats were, for example, observed in simulations of the flow over periodic hills [15] at the windward face of the smooth constriction. Further discussion of splats in this type of flow can be found in [16]. Another configuration where splats and antisplats are relevant flow features is the recirculation and reattachment region of the flow behind a backward-facing step. In the reattachment region behind the step, the mean shear is found to be small compared to wall–parallel attached flow, so that this region may be considered almost free of shear, thus resembling the situation of a shear-free boundary. In the recirculation region, the mean flow is weak compared to the outer flow as well, so that it is reasonable to look for splats/antisplats also in this part of the flow.

In flows with mean shear, splats and antisplats have an impact on the turbulent boundary layer as they interact with other vortical structures[3]. In particular, they play a substantial role in the transport of scalars such as heat or pollutants [7], [17], [18].

This literature survey demonstrates that in the application domain of near-boundary fluid mechanics the phenomenon of splats and antisplats is an important feature of relevance for a multitude of research questions. It has the potential to yield a better understanding of the physics and to pave a way towards better models that represent these physics, for example in Reynolds-averaged closures. On this background, it is to be recognized that splats and antisplats constitute a difficult feature when occurring within a complex turbulent flow with abundant other motion around, so that there still is no objective definition nor a robust method of detection, i.e., extraction, of this type of feature.

With the primary target users for our technique being engineers researching fluid mechanics, we propose a method which enables experts to investigate splats and antisplats directly from simulation results. With a clear spatial extent of these flow features, experts may study splats and antisplats together with their impact on turbulent flows in terms of transport, heat transfer or pressure fluctuations on the boundary. Also, the visualization of these phenomena provides a tool for experts to better understand the distribution and intensity of these events. Furthermore, a 3D visualization of splats and antisplats allows experts to study the

structure of these events and relate these phenomena to other flow features, e.g., vortices.

2.2 Characteristics and Definition

Consider a flow domain $D \subset \mathbb{R}^3$ with boundary ∂D. Based on the work of Perot and Moin [1], we define splat and antisplat events within D close to part of the boundary $B \subset \partial D$ as flow regions $S_R \subset D \times T$, where $T \subset \mathbb{R}$ denotes the time domain. These regions depict a flow volume integrated over time in domain D. In the present work, we assume B to be a flat boundary and the flow to be incompressible.

We propose the following conditions for S_R to be a splat on B:

1) Given an offset surface B^ϵ with a (very small) offset distance $\epsilon > 0$, the offset surface intersects with the splat, i.e., $S_R \cap B^\epsilon \neq \emptyset$.
2) The region $S_R \cap B^\epsilon$ is a connected space.
3) $\forall \mathbf{x} \in S_R$: A fluid volume moving towards B along the flow trajectory $p(\mathbf{x})$ with $p \subset S_R$ undergoes a specific type of deformation, it is stretched in tangential planes parallel to B while being compressed in normal direction.
4) $\forall t \in T$: Given a closed curve equivalent to the outer bound of $S_R \cap B^\epsilon$, the tangential velocity field on the curve should have a radial flow pattern, thus implying a positive Poincaré-Hopf index [19].

For an antisplat the direction of the velocity field is inverted with the corresponding modifications in Conditions 3) and 4).

From Conditions 1 and 2, we conclude that it is sufficient to identify splat and antisplat candidates at the boundary, i.e., in the offset plane, by identifying suitable regions $S \subset S_R \cap B^\epsilon$. Condition 3 is equivalent to observing that fluid elements approaching the wall experience a particular type of strain in case they are part of a splat, so that the deformation tensor is used as a suitable indicator in our detection method. Splat and antisplat events S_R can then be obtained via backward and forward integration of these candidates, utilizing S as seeding area. As we are interested in the splat and antisplat phenomena as such, it is appropriate to limit the backward/forward integration. Especially in turbulent flow, the integration of a fluid volume over a long time period may become a difficult task with little value to visualizing the process itself.

3 RELATED WORK

Splats and antisplats as features lacking a clear definition in fluid dynamics literature necessitate a discussion of previous studies concerned with near-wall flow dynamics and feature extraction.

3.1 Pathline-Based Methods

Salzbrunn et al. introduced the notion of streamline and pathline predicates in [20] and [21], respectively. In their definition, a line predicate is a Boolean function on streamlines or pathlines which determines if a line has a user-defined property. In their work, Salzbrunn et al. [21] also discuss unsteady flow structures. These are partitions of the set of pathlines constructed by combining pathline predicates based on Boolean algebra. With this in mind, it is natural to interpret splat and antisplat events as flow structures. A suitable collection of pathline predicates based on our splat definition should provide an appropriate approach to splat detection. The major drawback of this idea is that pathline predicates (and pathline-based approaches in general) require the prior computation of pathlines. As splats and antisplats can be small in scale, a dense seeding of the pathlines is unavoidable—leading to high computing cost. The high cost and the identification of suitable predicates for these fuzzy features make this approach challenging and impracticable for large datasets.

3.2 Fuzzy Feature Extraction

In their study, Dutta and Shen [22] present a method for the extraction of features where no clear definition is known. Based on a time-varying dataset they derive a description of the data as a Gaussian mixture model. With additional input of an expert and the corresponding Gaussian mixture model, their method achieves reliable extraction and tracking. Dutta and Shen showed that their method is suited for the extraction and tracking of fuzzy flow features. Although—with some adjustments and incorporation of our definition—their method could be applicable for splat detection, our goal in the present study is a fully automated splat detection based on our definition.

3.3 Coherent Structures

A common method that can be applied to the analysis of the near-wall flow dynamics is the analysis of Lagrangian coherent structures (LCS). In practice, these methods have proven to be very versatile in the analysis of turbulent flows. They provide strong indications of barriers separating regions of different behavior in time-dependent flow fields. A large number of studies addressing the mathematical foundations, computation, and applications of Lagrangian coherent structures are presented in the survey by Haller [23]. In general, LCS can be interpreted as the time-dependent analogy to vector field topology. As current methods extract LCS in a way that includes small-scale as well as large-scale features, clutter becomes challenging, especially with increasing turbulence. A hierarchy of Lagrangian coherent structures is not inherent, and therefore filtering on the basis of relevance is problematic.

Closely related to Lagrangian coherent structures, Froyland and Padberg [24] introduced a probabilistic approach for the detection of almost-invariant sets within the flow. These are regions of the flow that do not mix over a finite time span. Therefore, these structures describe regions enclosed by LCS. Splats and antisplats being off-wall fluid impinging on and separating off a surface infers a close relationship between these events and almost-invariant sets. Yet—like LCS—almost-invariant sets do not provide an inherent hierarchy and thus filtering is problematic. Especially in turbulent flows, this leads to a large amount of clutter.

3.4 Attachment and Separation

Methods for the analysis of attachment and separation in flows are related to our splat definition. Although such
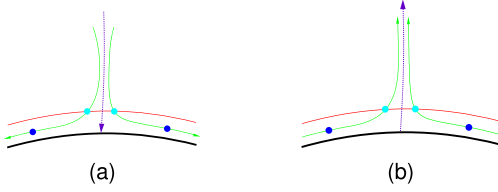
Fig. 2. Surface FTLE scheme of flow near the boundary. The flow trajectory (green) is integrated from starting points (cyan) at offset surface (red) forward (a) and backwards (b) in time. The end points are stored within the flow map.

methods have been presented for unsteady flow fields [25], [26], they focus on the analysis of Lagrangian coherent structures on the surface, or—in case of steady flows—on attachment and separation lines [27]. In contrast, splat and antisplat events are features with a spatial extent.

Nevertheless, we employ ideas introduced by Garth et al. [25]. They compute the rate of attachment and detachment on surface areas based on *Finite-Time Lyapunov Exponents* (FTLE) as introduced by Haller et al. [28]. Let $\Phi_{t_0}^t(\mathbf{x}_0) : D \to D$ denote the flow map of a time-dependent velocity field $\mathbf{v}(\mathbf{x}, t)$ that maps the initial position $\mathbf{x}_0 \in D$ of a mass-less particle at time $t_0 \in T$ to its position at time $t = t_0 + \tau$ with the integration length τ. $\text{FTLE} : D \times T \times I \to \mathbb{R}$ is then defined for the set of possible integration lengths $I \subset \mathbb{R}$ as follows:

$$\text{FTLE}(\mathbf{x}_0, t; \tau) = \frac{1}{|\tau|} \ln \sqrt{\lambda_{\max}\left[\nabla \Phi_t^{t+\tau}(\mathbf{x}_0)^T \nabla \Phi_t^{t+\tau}(\mathbf{x}_0)\right]},$$
(1)

with the spatial gradient of the flow map $\nabla \Phi_t^{t+\tau}(\mathbf{x}_0) \in \mathbb{R}^{3\times 3}$, $(.)^T$ denoting the transposed matrix, and $\lambda_{\max}[.]$ the largest eigenvalue.

While FTLE in general is used to analyze flow behavior in the entire domain, surface FTLE by Garth et al. [25] adapts this concept: Let an object embedded in the domain D have a smooth boundary surface B in terms of differential geometry. For this surface B, an offset surface $B^\epsilon := \mathbf{x} + \epsilon \mathbf{n}(\mathbf{x}), \mathbf{x} \in B$ can be defined, where $\mathbf{n}(\mathbf{x})$ is the surface normal to B at position $\mathbf{x}$ and $\epsilon > 0$ is the offset. For sufficiently small ϵ, the offset surface itself is smooth [29]. Applied to the offset surface $B^\epsilon \subset D$, FTLE only measures the separation of particles originating from B^ϵ. Note that the gradient computation is restricted to the (tangential) offset surface. The interpretation suggested by Garth et al. [25] is straight forward. Attachment implies high FTLE values obtained by forward integration, since the flow started near the surface is most commonly separated by the boundary. High FTLE values obtained by backward integration imply detachment. (see Fig. 2)

Garth et al. [25] showed that the FTLE computation works well for nearly laminar flows. Applying this approach to turbulent flows harbors some difficulties. In contrast to turbulent flows, the separation of two fluid particles is slow in laminar flows. As a result, particle separation is mainly governed by the boundary in the flow direction. This makes the method fairly robust under changes of τ for virtually laminar flows. In turbulent flows, integration seeded near the surface may result in an inaccurate characterization of the flow. Small scale phenomena near the boundary surface

like vortices and an unclear main flow direction in a local region near the boundary make the interpretation of high particle separation ambiguous. In addition, antisplats and splats are interacting phenomena. As a result, particles being separated by impinging on the boundary surface can converge within an antisplat after further advection by increasing τ and *vice versa*. Further taking into account, that the velocity in turbulent flows may be very inhomogeneous, a global integration time τ is not appropriate for a robust splat and antisplat detection.

3.5 Local Approach to FTLE

As stated in the previous subsection, a global integration time yields issues when analyzing attachment and separation in turbulent flows with the technique Garth et al. [25] introduced. Therefore we require a discussion on a concept introducing a local approach to FTLE.

Kasten et al. [30] propose an alternative method in the computation of FTLE-fields based on the local deviation of the neighborhood along individually processed pathlines instead of the flow map—namely localized FTLE. Considering a pathline $p(\tau) = p(\mathbf{x}_0, t_0; \tau)$, the deviation of trajectories of an infinitesimally close particle is governed by the spatial gradient of the velocity field $\mathbf{v}(\mathbf{x}, t)$ along the pathline. We denote this infinitesimally close (perturbed) particle as $\mathbf{y} := \mathbf{x}_0 + \boldsymbol{\sigma}(t)$, where $\boldsymbol{\sigma}(t) \in \mathbb{R}^3$ is a time-varying perturbation vector following $\|\boldsymbol{\sigma}(0)\| \to 0$. The temporal evolution of the deviation $\sigma(t)$ is given by the equation

$$\dot{\sigma}(t) = \prod_{p(\tau)} \nabla \mathbf{v}(\mathbf{x}, t)\sigma(t)^{dt}.$$
(2)

Note that Equation (2) employs a product integral over the pathline $p(\tau)$ governing the evolution of the spatial gradient. For very small values of t the gradient can be approximated by a constant matrix $\nabla_0 = \nabla \mathbf{v}(p(0), t_0)$. The solution of the equation for very small values of t then is

$$\sigma(t) = \exp(\nabla_0 t)\sigma(0).$$
(3)

Kasten et al. [30] applied this approximation for short time spans repeatedly along the pathline $p(\tau)$ at equidistant sample points $\mathbf{x} \in p(\tau)$ forward in time, obtaining the equation

$$\sigma(\tau) = \left[\prod_{i=N-1}^{0} \exp(\nabla_i \Delta_t)\right] \sigma(0),$$
(4)

with the number of discrete time steps N and the (small) sample length Δ_t. Note that $\Delta_t \cdot N = \tau$ and $\nabla_i = \nabla \mathbf{v}(p(i\Delta_t), i\Delta_t)$—the Jacobian of the velocity field at the ith sample point—apply. The matrix

$$\Psi_{t_0}^t(\mathbf{x}_0) := \prod_{i=N-1}^{0} \exp(\nabla_i \Delta_t)$$
(5)

then is a mapping of the neighborhood at point $\mathbf{x}_0$ to deviation after advection over the timespan τ. It is similar to the flow map gradient introduced earlier. Localized FTLE is computed here analogous to FTLE:

$$\text{L-FTLE}(\mathbf{x}_0, t; \tau) = \frac{1}{|\tau|} \ln \sqrt{\lambda_{\max}\left[\Psi_t^{t+\tau}(\mathbf{x}_0)^T \Psi_t^{t+\tau}(\mathbf{x}_0)\right]}.$$
(6)

This approach to the computation of FTLE allows us to analyze the flow dynamics locally and solve the issues occurring with the application of a global time span in turbulent flows. As there is no inherent correlation between the FTLE-field and the splat/antisplat regions, we develop a method based on the concepts of surface FTLE and localized FTLE in conjunction with our splat definition.

4 METHOD

In the following, we describe the method for the detection of splats. For antisplats, the same steps are used with straightforward changes of sign in the appropriate steps, e.g., replacing forward integration by backward integration. Our detection method extracts splat regions on the offset boundary surface as this is sufficient in terms of our splat definition. We interpret splat and antisplat events in the context of three-dimensional turbulent flows as special cases of attachment and detachment on the surface structure. Therefore, our first goal is a characterization of fluid element behavior near the boundary. Based on these characteristics, we derive indicators for the splat and antisplat detection and present an algorithm for the detection of these phenomena.

The idea of our method is to evaluate the strain of an isotropic fluid volume approaching the boundary according to Condition 3 of the splat definition. It is devised here for a flat boundary surface. We first define the offset boundary surface $B^\epsilon := \mathbf{x} + \epsilon \mathbf{n}, \mathbf{x} \in B$ of boundary B. As we are interested in the attachment in a turbulent flow field, it is necessary to exclude phenomena which could lead to ambiguous results, such as vortices or detachment. Our solution to this problem is to solely consider the flow direction of the particles moving towards the boundary surface by introducing a termination criterion for the advection. The particle is advected as long as it approaches the boundary in a monotonic manner (see Fig. 3a). Seeding on the offset surface B^ϵ with the boundary normal $\mathbf{n}$ directed into the flow, the massless particle advects as long as the condition

$$\forall \mathbf{x} \in p(\tau) : \langle \mathbf{v}(\mathbf{x}, t), \mathbf{n} \rangle \leq 0 \tag{7}$$

holds, with $\langle .,. \rangle$ denoting the scalar product. As a result, particle separation is mainly governed by the geometry of the boundary surface B.

Note that the termination criterion yields trajectories with varying integration times. In addition to the drawbacks of (classical) surface FTLE discussed in Section 3.4, flow maps and their linearization require a global integration time by definition [28]. Consequently, we employ localized FTLE ideas described in Section 3.5 to analyze the flow dynamics along isolated trajectories independently.

After advecting massless particles seeded on the offset surface B^ϵ, we sample the computed pathlines and apply Equation (5) for varying time steps. We obtain $\Psi_{t_0}^{\bar{t}}(\mathbf{x}_0)$ where $\bar{t}$ is the maximum time covered by an individual path line using forward integration. We employ central differences for an approximation of the Jacobian ∇_i and a fixed time Δ_t between two consecutive samples with a maximum integration time τ.

We then obtain the *right Cauchy-Green* tensor as follows:

$$C^{\bar{t}}(\mathbf{x}_0) := \Psi_{t_0}^{\bar{t}}(\mathbf{x}_0)^T \Psi_{t_0}^{\bar{t}}(\mathbf{x}_0), \tag{8}$$
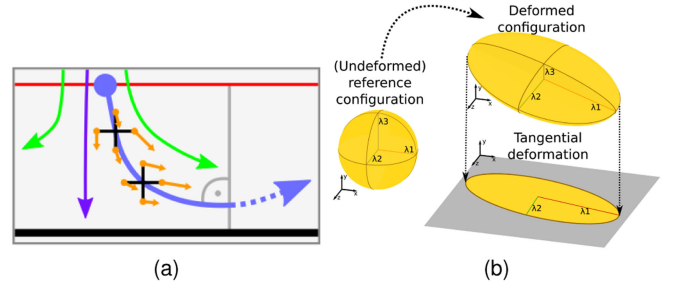

Fig. 3. Illustration of the splat detection method. (a) Localized surface characterization scheme employed in our method. The blue trajectory shows a path line terminated under the condition stated in Equation (7). With the indicated main flow direction (purple) and the attachment flow trajectories (green), the pathline (blue) seeded at the offset surface (red) is sampled for the computation of the Jacobian. (b) This image shows the tensor glyph of the strain of an isotropic fluid volume in a reference configuration, after advection, and subsequently projected onto the surface. Note that the eigenvalues and eigenvectors vary in every step.

where $C^{\bar{t}}$ denotes the right Cauchy-Green tensor obtained by forward integration. In the case of antisplat detection, we compute the sampling trajectory via integration backward in time. Note that in this case the instantaneous gradients at the sample points are computed with the inverted velocity vectors.

In the remainder of this paper, we refer to $C^{\bar{t}}$ for both forward and backward integration, as C. The right Cauchy-Green tensor is a classic measure of strain and is always symmetric and positive definite [31]. In general, second order strain tensors characterize changes of material elements during motion from a reference configuration (see Fig. 3b). By doing this, the distance of two neighboring points of the material element is altered. Note that strain tensors do not include information about rotation or translation [31]. These material elements correspond to fluid elements of the turbulent flow. The right Cauchy-Green tensor C obtained by our method characterizes the deformation of a fluid element along a trajectory. FTLE only takes the largest eigenvalue of C into account, which corresponds to the strongest elongation of a fluid element.

Here, we focus on the entire right Cauchy-Green tensor C, as it contains further information for the characteristics of the flow. While usual FTLE can be interpreted as the maximum separation of two particles, the whole tensor C can be interpreted as the deformation pattern of a flow volume. We denote the eigenvalues of C by $\lambda_0, \lambda_1, \lambda_2$, where $\lambda_0 \leq \lambda_1 \leq \lambda_2$. A value of $\lambda_i = 1$ indicates no deformation while values of $\lambda_i > 1$ and $\lambda_i < 1$ characterize elongation and compression for their corresponding dimension in eigenspace, respectively. With this in mind, a fluid volume approaching the boundary and thus being stretched in tangential direction and compressed in normal direction characterizes an attachment process. When a fluid volume approaches the boundary, we expect the stretching to be highly directional. A fluid volume with a dominant normal velocity component is expected to stretch uniformly on the tangent plane. This behavior can be characterized by the eigenvalues of the right Cauchy-Green tensor with an orthonormal basis corresponding to the surface tangent plane and normal.

The computed tensor C does not necessarily fit this condition as the deformation is solely governed by the flow

where fluid volumes may interact. Therefore, we project the right Cauchy-Green tensor onto the offset surface B^ϵ. To capture the tangential deformation, we introduce the tangential right Cauchy-Green tensor $C_t \in \mathbb{R}^{2\times2}$ as

$$C_t(\mathbf{x}_0) := M^T C(\mathbf{x}_0) M, \tag{9}$$

with $M \in \mathbb{R}^{3\times2}$ and its transpose $M^T \in \mathbb{R}^{2\times3}$ constituting an orthonormal basis of the tangent plane. The matrix M is constructed as follows:

$$M := \begin{bmatrix} \mathbf{a} & \mathbf{b} \end{bmatrix}, \tag{10}$$

where $\mathbf{a}(\mathbf{x}_0)$ and $\mathbf{b}(\mathbf{x}_0)$ are vectors in the tangent plane satisfying $\langle \mathbf{a}, \mathbf{b} \rangle = 0$ at position $\mathbf{x}_0$. Additionally, we introduce the normal right Cauchy-Green tensor $C_n \in \mathbb{R}^{1\times1}$ as

$$C_n(\mathbf{x}_0) := \mathbf{n}^T C(\mathbf{x}_0) \mathbf{n}, \tag{11}$$

with the surface normal $\mathbf{n}$. The eigenvectors $\gamma_{t_0}, \gamma_{t_1}$ of C_t and the normal $\mathbf{n}$ define an orthonormal basis. Considering the interpretation of the corresponding eigenvalues $\lambda_{t_0}, \lambda_{t1}$ and λ_n as indicators for elongation and compression as well as the expected behavior of a fluid volume respecting Equation (7), we consider the following cases:

1) $\lambda_n \leq \lambda_{t_0} \leq \lambda_{t_1} < 1$: The flow is converging. As we are not interested in converging flow behavior, these cases are discarded.
2) $\lambda_n < \lambda_{t_0} < 1 < \lambda_{t_1}$: The flow is diverging in one tangent direction and converging in the other. In a radial flow, we conclude that this is the result of deceleration of the fluid volume in flow direction with an expansion orthogonal to the flow direction.
3) $\lambda_n < 1 < \lambda_{t_0} \leq \lambda_{t_1}$: The flow stretches in both tangential directions when approaching the boundary. In a radial flow, we conclude that this is the result of either an acceleration of the flow volume with an elongation orthogonal to the flow direction, or a uniform radial elongation of the volume.
4) $\max\{\lambda_{t_0}, \lambda_{t_1}\} < \lambda_n$: In these cases, we assume that no energy is transferred from the normal velocity component to the tangential components.

As stated in Section 2, splats are regions of stagnation. Within an incompressible fluid, the bulk flow impinging on the boundary has to transfer its normal velocity into a tangential velocity. With this in mind, the velocity magnitude must be minimal in the center of the splat (see Fig. 1). Resulting from the fluid displacement, the velocity magnitude is expected to increase with increasing distance from the center of the splat. We conclude that Case 3) fits our definition and the expected behavior of a splat event. It covers the scenario of a dominant normal velocity component causing a radial extension of the flow as well as an acceleration of the flow as it moves away from the center. This is also valid for antisplats, as they are computed analogously using backward integration. Based on Case 3), we now define a splat region $S_i \subset B^\epsilon$ to be a simply connected component satisfying

$$\forall \mathbf{x}_0 \in S_i : \lambda_{\min}[C_t(\mathbf{x}_0)] > 1 \wedge \lambda[C_n(\mathbf{x}_0)] < 1. \tag{12}$$

As simply connected regions in B^ϵ are inherently disjoint, it follows that splat regions are disjoint regions. Also, from the abort criterion follows that splat and antisplat regions are disjoint, as it cannot be valid for backward and forward integration at the same point $\mathbf{x}_0$.

Algorithm 1. Splat Detection

1: **Input:** velocity field $\mathbf{v}(\mathbf{x}, t)$ with flat surface of interest, offset distance ϵ, sample length Δ_t, max. integration time τ, start time t_0
    Output: splat regions $S \subset B^\epsilon$
2: **compute:** simplicial offset surface B^ϵ
3: **(optional):** subdivide surface
4: $\lambda[] \leftarrow 0; C_n[] \leftarrow 0;$
5: **for all** $\mathbf{x} \in B^\epsilon$ **do**
6: $\quad$ $\mathbf{p} \leftarrow (\mathbf{x}, t_0); t \leftarrow t_0;$ samples[].push($\mathbf{p}$);
7: $\quad$ **while** $t < t_0 + \tau$ **and** $\langle \mathbf{v}(\mathbf{p}), \mathbf{n} \rangle \leq 0$ **do**
8: $\quad\quad$ **compute** num. integration RKDP($\mathbf{p}, \Delta_t$) $\rightarrow \mathbf{p}$
9: $\quad\quad$ $t \leftarrow t + \Delta_t;$ samples[].push($\mathbf{p}$)
10: $\quad$ **end while**
11: $\quad$ $\Psi \leftarrow I$ {identity matrix $\mathbb{R}^{3x3}$}
12: $\quad$ **for all** $\mathbf{p} \in$ samples[] **do**
13: $\quad\quad$ $J \leftarrow exp(\nabla \mathbf{v}(\mathbf{p})\Delta_t)$
14: $\quad\quad$ $\Psi \leftarrow J \times \Psi$
15: $\quad$ **end for**
16: $\quad$ $C_t \leftarrow M^T[\Psi^T\Psi]M$ {according to Eq. 8, 9}
17: $\quad$ $C_n[\mathbf{x}] \leftarrow n^T[\Psi^T\Psi]n$
18: $\quad$ $\lambda[\mathbf{x}] \leftarrow \lambda_{min}(C_t)$
19: **end for**
20: **initialize** Union-Find(B^ϵ) data structure (UF)
21: **for all** $\mathbf{x} \in B^\epsilon$ **do**
22: $\quad$ **for all** adjacent points $\mathbf{y} \in B^\epsilon$ **do**
23: $\quad\quad$ **if** $min(\lambda[\mathbf{x}], \lambda[\mathbf{y}]) > 1$ **and** $max(C_n[\mathbf{x}], C_n[\mathbf{y}]) < 1$ **then**
24: $\quad\quad\quad$ $merge(\mathbf{x}, \mathbf{y})$
25: $\quad\quad$ **end if**
26: $\quad$ **end for**
27: **end for**
28: **compute** tangential velocity field at time t_0
29: **compute** singular points on B^ϵ of tangential velocity field
30: **for all** sets $\mathcal{S}$ in UF **do**
31: $\quad$ **if** $|\mathcal{S}| > 1$ **and** Eq. 13 is valid **then**
32: $\quad\quad$ **add** splat region $\mathcal{S}$
33: $\quad$ **end if**
34: **end for**

The segmentation for the extraction of the splat regions in B^ϵ is straightforward. In this work we employ a segmentation approach utilizing a union–find structure (see lines 20-27 of Algorithm 1). To verify a radial flow pattern on the boundary surface, we need to ensure a positive Poincaré-Hopf index for the outer bounds of the splat regions (see Condition 4) in Section 2). Therefore, we require the detected splat regions to satisfy

$$\exists \mathbf{x}_0 \in S_i : \|\mathbf{v}_{B^\epsilon}(\mathbf{x}_0, t)\| = 0, \tag{13}$$

where $\mathbf{v}_{B^\epsilon}(\mathbf{x}_0, t)$ is the velocity field $\mathbf{v}(\mathbf{x}_0, t)$ at seeding time t projected onto the offset surface B^ϵ. From the eigenvalue criterion and Equation (13) it follows that the Poincaré-Hopf index is positive. As we cannot ensure a positive Poincaré-Hopf index for splat regions intersecting the bounds of B^ϵ,

only regions with a neighborhood contained in B^ϵ are required to satisfy Equation (13). Note that the presented method is applicable to a discrete velocity field and a (simplicial) grid as the offset surface. Seeding of the trajectories for the detection method is then performed on the vertices of the offset plane. When studying FTLE on flow embedded surface structures, Garth et al. [25] recommend subdividing the offset surface structure yielding a higher mesh resolution for a better approximation. In our method, we apply linear interpolation of the edges and a 4-fold subdivision of the triangles in the offset surface. The necessity of a subdivision depends on the given grid resolution. Therefore, this step is optional.

The summary of our method is presented in Algorithm 1. Note that the extraction of antisplats requires integration backward in time and the gradients are computed with inverted velocity vectors.

5 VISUALIZATION

In our visualization approach, we employ existing techniques suitable for the presentation of the extracted flow features. As the splats and antisplats have a direct impact on the wall, it is desirable to provide an overview of their distribution and intensity mapped to the (offset) surface. Therefore, we propose a color mapping scheme for this task. This scheme allows for an intuitive evaluation of the detected events with no overlap. Additionally, we employ a path line visualization technique with an emphasis on structural and spatial perception, allowing the expert to study interactions of splats, antisplats, and other flow features, e.g., vortices.

5.1 Splats and Antisplats on a Surface

For the first visualization scheme, we perform a direct visualization of splat and antisplat events by coloring the extracted regions of the offset boundary surface B^ϵ. Note that we consider the flat offset surface to be triangulated with uniformly sized cells. As it is desirable to visualize both, splats and antisplats, we propose a coloring scheme to color both structures with an emphasis on their relative strength. We base the measure of the strength of a splat on the volume flux in normal direction through the splat region, here the volume flux Q passing through the splat region within the offset plane B^ϵ close to the boundary B. As the time spans vary for each trajectory, we approximate the throughput using the velocity field $\mathbf{v}(\mathbf{x}, t)$ at time t_0. The volume flux through a cross-section area A can be obtained by $Q = uA$, where u is the mean velocity of the flow normal to A. For our visualization, a sufficient discrete approximation of the volume flux for a splat at time t_0 only considering the normal flow direction results in for following computation for the splat with index i:

$$Q_i = \alpha \sum_{\mathbf{x} \in S_i} |\langle \mathbf{v}(\mathbf{x}, t_0), \mathbf{n} \rangle| \qquad (14)$$

for splats and antisplats. Here, we apply the approximations $u \approx [\sum \mathbf{v}_n]/|S_i|$ and $A \approx \alpha|S_i|$. The area element α is constant and can be approximated by the area of the Voronoi cells of the offset surface. which are valid for sufficiently dense uniformly distributed points with in the offset plane.
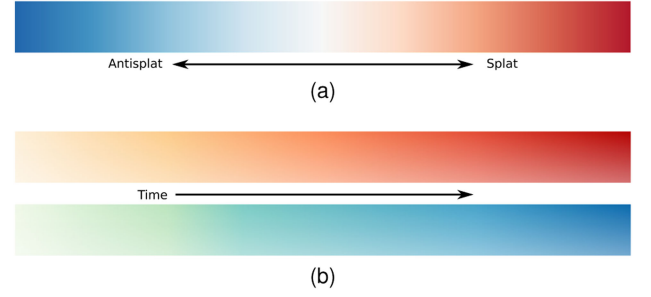

Fig. 4. Color Mapping scheme employed in our splat and antisplat visualization. (a) A diverging color map for splats and antisplats superimposed onto the scalar field $\psi(\mathbf{x}, t)$ defined on the offset surface. (b) This image shows the continuous color maps encoding time t for the path line visualization of splats (top) and antisplats (bottom).

With the strength of the individual splats and antisplats we can compute a splat-antisplat scalar field $\psi(\mathbf{x}, t)$ as follows. We initialize $\psi(\mathbf{x}, t) = 0$ for every point x in the offset plane B^ϵ. For all splats S at time t_0 we set:

$$\forall i \forall \mathbf{x} \in S_i : \psi(\mathbf{x}, t_0) = Q_i(S_i) \qquad (15)$$

and for antisplats S^A

$$\forall i \forall \mathbf{x} \in S_i^A : \psi(\mathbf{x}, t_0) = -Q_i(S_i^A). \qquad (16)$$

We then divide the results of the Equations (15) and (16) by the maximum volume flux to obtain a normalization to the interval $[-1, 1] \in \mathbb{R}$. Note that the constant α becomes redundant by this step. As S and S^A are disjoint, $\psi(\mathbf{x}, t)$ carries the information of both fields, where positive values correspond to splats and negative values to antisplats. $\psi(\mathbf{x}, t_0)$ then is superimposed on a color map, where both events are displayed and the maximum intensity of a splat/antisplat can be encoded by a color scheme. The color map is hereby defined on the offset surface B^ϵ. For the visualization of $\psi(x, t_0)$ we use the divergent color map shown in Fig. 4a in accordance with the studies of Moreland [32].

A drawback of this coloring scheme is that the perception of low-intensity splat regions can be problematic and lead to the events being barely visible. To counteract this, the user can add red and blue borders to the splat and antisplat regions respectively. This maintains the intuition where saturation correlates with the intensity but allows low-intensity splats/antisplats to be easily identified. (cf. Fig. 18)

5.2 Structural Visualization

In addition to direct visualization of the region on B^ϵ, we employ pathlines to visualize the splat and antisplat events in the three-dimensional domain. Pathlines can be obtained by a straightforward and robust computation also in highly turbulent flows. The time-dependent nature of pathlines provides direct visualization of massless tracer particles resulting in a splat or antisplat event. In addition, one can easily track the origin and further advect such a particle. We seed bulk pathlines on the extracted splat and antisplat regions. As the splat and antisplat regions are cross sections of the flow regions S_R with the offset surface B^ϵ, both forward and backward integration seeded at B^ϵ is needed to fully visualize a splat or antisplat. Note that for splats and antisplats, the emphasis is on backward and forward

integration, respectively. This way pathlines of splats show the advection of particles onto the surface and pathlines of antisplats depict the advection of particles away from the surface, passing through the offset surface B^ϵ. Forward integration and backward integration for splats and antisplats, respectively, should be short because particles *splatting* onto the surface can eventually be caught in an antisplat event as time progresses and vice versa, which could result in an ambiguous visualization.

As we are interested in the flow regions $S_R \subset D \times T$ capturing splatting and antisplatting, sparsely seeded pathlines are not suitable for their visualization. With the computation of large quantities of pathlines per splat, clutter and the loss of spatial information of the trajectories disturbs the visualization. An efficient method for rendering bulks of pathlines in the three-dimensional domain was proposed by Eichelbaum et al. [33]. This method was successfully employed in tractography visualization of dense line bundles and runs in real time. In their technique, Eichelbaun et al. used ambient occlusion on pathlines to improve the spatial and structural perception of individual lines and also bundles of lines. To fully exploit this visualization scheme, the seeding of the trajectories is very dense and equidistant. An adequate coloring of the pathlines can encode the nature of the rendered event in addition to temporal information. This allows us, to seed dense pathlines without losing spacial perception of the trajectories (cf. Fig. 17).

In his study, Moreland [32] also presented a suitable approach to coloring sequential data. He states that saturation is appropriate for continuous color maps as shown by Rheingans [34]. The color maps for splats and antisplats are shown in Fig. 4b respectively.

With an increasing density of unique phenomena, it becomes more challenging to distinguish individual splats and antisplats. To counteract this, the user can define regions which should be highlighted with a different coloring scheme (cf. Fig. 21).

6 ANALYTICAL FLOW

In this section, we apply our method to artificially generated steady flow fields with a free-slip boundary condition. Our goal is to validate the method and to evaluate its reliability for different prototypic constellations. For this purpose, we developed a tool—the splat generator—for the creation of artificial flows containing various phenomena. The splat generator is based on individual flow elements i.e., potential vortices, stagnation point flows and sources. These flow elements can be combined and arranged as required. Here, we consider an $x - z$-plane at $y = 0$ with normal vector $\mathbf{n}(\mathbf{x}) = [0, 1, 0]$ directed towards the flow. We focus on the stagnation point flow elements directed in negative y-direction, which we interpret as ideal splat events.

The stagnation point flow element has the potential $\phi = \frac{a}{2}(x^2 - 2y^2 + z^2)$ where x, y and z are the domain coordinates and a is the strength of the splat. A negative value for a is used to model an antisplat. The velocity field is then computed from the gradient of ϕ (cf. 10.71 in [35], e.g.,) yielding

$$u = \frac{a}{2}(x - p_x), \quad v = -a(y - p_y), \quad w = \frac{a}{2}(z - p_z). \quad (17)$$
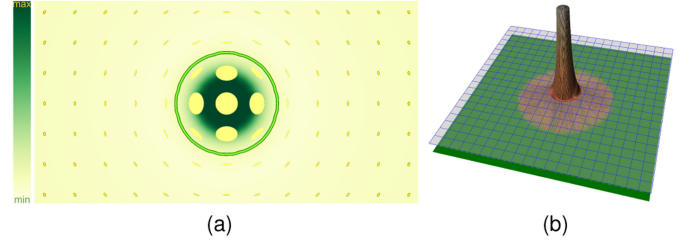

(a)   (b)

Fig. 5. (a) Minimal eigenvalues of the tangential Cauchy-Green tensor. This figure shows the color mapping (left) of the minimal tangential Cauchy-Green tensor superimposed onto the offset surface (x-z-plane) for a simple splat. In addition, we illustrate the tensor glyphs of the projected Cauchy-Green tensor. The green isoline represents the location where the minimal eigenvalue of the tangential Cauchy-Green tensor is 1. (b) Simple splat visualization. This figure shows the simple splat computed on the offset surface (latticed) of the boundary structure (green). The computed splat region within the offset surface is used to generate the splat volume visualization according to Section 5.

In addition to the position $\mathbf{p}$ of the stagnation point and the strength a, the user can adjust the splat size r. The splat generator models the size by introducing a sphere with a radius equal to r. Outside the sphere, the field is attenuated to decay with r^{-2}. Note that the $y-$component of the position vector $\mathbf{p}$ is always zero. To assess whether the new method is also able to distinguish between (anti-)splats and other flow structures we occasionally add additional potential vortices rotating around a straight line parallel to the z-axis. A vortex generated by the splat generator is defined by the position of the vortex core line $\mathbf{g} = \mathbf{p}_v + o\mathbf{e}_z$, the vortex strength a_v and the vortex size r_v, where $\mathbf{e}_z = [0, 0, 1]^T$ and $o \in \mathbb{R}$. The user can modify the position of the axis $\mathbf{p}_v$ as well as the vortex strength a_v and size r_v.

6.1 Simple Splat

In a first step, we apply our method to a field containing only a single stagnation point flow with positive strength. For this case, we chose a splat at the origin $\mathbf{p} = [0, 0, 0]^T$ with strength $a = 1.0$ and a splat size $r = 1.0$. The domain bounds are $[-4, 4] \times [0, 6] \times [-4, 4]$ with a grid of $40 \times 40 \times 40$ points. The analysis of the parameters and a guideline to their choice will be provided in the next section. For this exemplary case of a simple stagnation point flow, we chose an offset distance of $\epsilon = 0.5$ and a maximum integration time $\tau = 2$. Note that the rather high offset distance is chosen for illustrative purposes and does not affect the result significantly for this simple configuration. The sample length is chosen to be $\Delta_t = 0.1$ and three subdivisions were employed resulting in a simplicial offset surface containing 97969 grid points.

To further illustrate the tangential Cauchy-Green tensor for a simple stagnation point flow, we use ellipsoid tensor-glyphs as shown by Kindlmann [36] in Fig. 5a. The two eigenvalues in the tangential plane are highly isotropic in the center. The values of the minimal tangential eigenvalues in Fig. 5a show that the tangential eigenvalues within the splat are above one. With increasing distance to the core, the tensor glyphs become increasingly anisotropic where at some point the minimal eigenvalue becomes smaller than one. After a further increase of the distance, the glyphs show an isotropic structure approaching eigenvalues of one.

The resulting visualization of the extracted splat region is shown in Fig. 5b. We computed the splat region within the
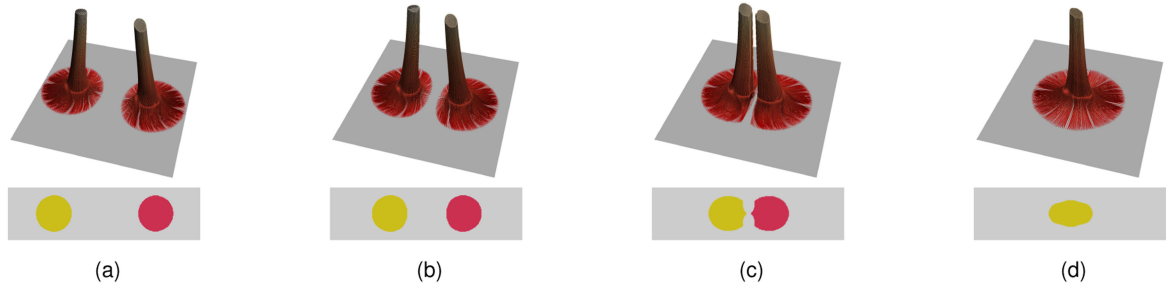
Fig. 6. Two Splat regions detected on the offset surface. These figures show the splat regions (random colors) on the offset surface detected by our method. The stagnations point flows generated differ in their stagnation point location. Figure (a) shows a stagnation point distance $d = \|\mathbf{p_1} - \mathbf{p_2}\| = 4$. Figures (b), (c) and (d) show splats with the distances $d = 3$, $d = 2$, $d = 1$, respectively.

offset surface B^ϵ using our method. Within the extracted domain, we seeded streamlines and integrated these forward and backward. The seed points are equivalent to the subdivided offset boundary points covered by the detected splat region, for this case 2113 points in total. The computed trajectories were then visualized according to the scheme introduced in Section 5.

6.2 Splat-Splat Interaction

To study the behavior of the detection method for converging splat events, we applied our method to various configurations in the same domain as used in the previous section. We generated fields with two splats with different distances $d = \|\mathbf{p_1} - \mathbf{p_2}\|$ of the stagnation points $\mathbf{p}_1, \mathbf{p}_2$. Note, that the y-components are equivalent. Our goal is a reliable detection of distinct splats in spite of being geometrically close. For these cases, we apply the offset distance $\epsilon = 0.2$, maximum integration time $\tau = 2$, sample length $\Delta_t = 0.1$ and three subdivisions with different stagnation point positions. The resulting boundary splat regions and the corresponding three-dimensional visualization is shown in Fig. 6. The first case in Fig. 6a shows two splats with distance $d = 4$. As the splat size for the splats is $r = 1$, we do not expect interaction. When reducing the distance, the case of two splats being very close is shown in Fig. 6c. The distance for this case is $d = 2$ so that the splats are supposed to interact. The detected splats for this case differ in their structure, as the splat regions on the offset surface lose their anisotropic shape. Nevertheless, our method extracts two distinct splats even for this borderline case. Further reducing the distance leads to the splats intersecting. Fig. 6d shows that the intersecting splats are detected as a single splat by our method, which is desired.

6.3 Multiple Splats and Antisplats

In this subsection, we introduce antisplats to our method and increase the number of stagnations point flows. In addition, different splat strengths and sizes, as well as differing distances, are employed. Bearing in mind the results of Section 6.2, we avoid merging of splats and antisplats. We use the offset distance $\epsilon = 0.2$, maximum integration time $\tau = 2$, sample length $\Delta_t = 0.1$ and three subdivisions. We generate the phenomena in a way that there is no intersection among the expected (spherical) regions defined by the stagnation points $\{p_0, ..., p_n\}$ and the corresponding radii $\{r_0, ..., r_n\}$. The splat generator is set to the domain $[-5, 5] \times [0, 6] \times [-5, 5]$. The parameters used for the generation can be seen in Table 1.

Applying the new method with our visualization scheme to the resulting flow field yields the graphs shown in Figs. 7 and 8. A comparison of the generated splats in Table 1 and the resulting regions shows that the detected regions increase in size and intensity $\psi(\mathbf{x}, \mathbf{t_0})$ with increasing strength a and/or size r. Note that for splats $\psi(\mathbf{x}, \mathbf{t_0})$ approximates the product of the mean normal velocity u and the area A. Also $u \propto a$ and $A \propto r$. Therefore, from $\psi(\mathbf{x}, \mathbf{t_0})$ we cannot evaluate the impact of these properties separately. The shape of the detected region differs fundamentally from the shape resulting from an ideal simple splat (Section 6.1). We conclude that splats and antisplats interact within the

TABLE 1
Splats and Antisplat Parameters for the Synthesis of Flow
Fields for Validation

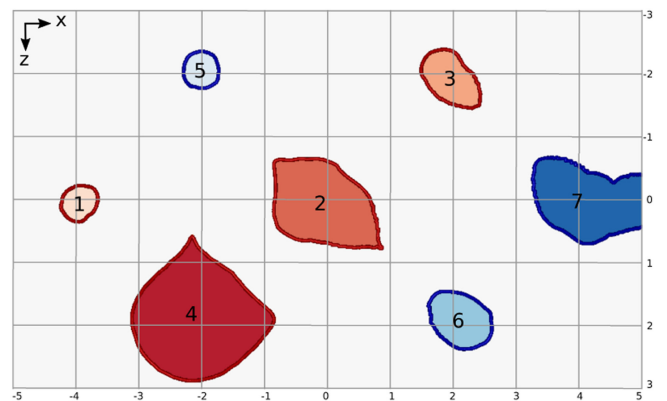| Index	Stag. point position $\mathbf{p}$	Strength a	Size r
1	$[-4.0, 0.0, 0.0]$	1.0	0.5
2	$[0.0, 0.0, 0.0]$	0.9	1.0
3	$[2.0, 0.0, -2.0]$	1.5	0.7
4	$[-2.0, 0.0, 2.0]$	0.8	1.3
5	$[-2.0, 0.0, -2.0]$	-1.0	0.5
6	$[2.0, 0.0, 2.0]$	-1.2	0.7
7	$[4.0, 0.0, 0.0]$	-1.5	1.0

Fig. 7. Multiple splats and antisplats detected and visualized by our method. This figure shows the resulting phenomena generated by the splat generator according to Table 1. We created seven stagnation point flows, with the first four being splats and the following three being antisplats. The detected splat regions are colored according to our visualization scheme with additional borders for improved visibility. The numbering of the regions refers to the index in Table 1.
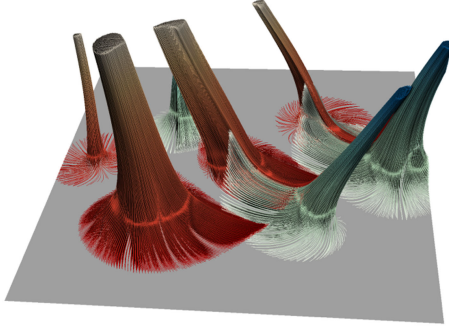
Fig. 8. Splats and Antisplats detected and visualized by the proposed method. This figure is the pathline visualization of the regions shown in Fig. 7 according to our visualization scheme for splats and antisplats.
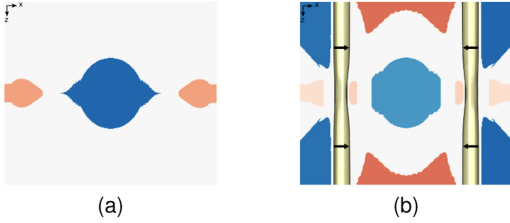

Fig. 10. Three-dimensional visualization of the detected splats and anti-splats. This image shows the pathline visualization of the splats and anti-splats in a flow field including vortices (yellow). The pathline seeding was performed on the vertices of the offset plane (two subdivisions). This flow field was used to create Fig. 9b.

(a)   (b)

Fig. 9. Splat and Antisplat regions with vortices. This image shows the splat regions on the offset surface (three subdivisions). (a) Regions found in a flow field containing two splats and one antisplat. (b) Result when supplementing this flow field by two vortices (yellow) generating further splat and antisplat regions, then detected by our method.

flow field, as the deformation of the regions appears to be directional. The isotropic tendencies of the detected regions do not occur near the center, which implies an acceleration of the flow in the direction of the opposing phenomenon. Fig. 8 highlights the interaction, as some particles involved in a detected splat form an antisplat after further advection.

6.4 Splats and Antisplat with Vortex

The third level of complexity in the validation cases is to create an amalgam of (anti)splats together and other flow features, so as to verify that the proposed scheme can, indeed, successfully distinguish between them and reliably extract the (anti)splats. To this end, we first generate three stagnation point flows in the domain with an extent of $[-5, 5] \times [0, 6] \times [-5, 5]$ and $40 \times 40 \times 40$ grid points. These are configured with the positions $\mathbf{p}_1 = [-4, 0, 0]$, $\mathbf{p}_2 = [4, 0, 0]$ and $\mathbf{p}_3 = [0, 0, 0]$. Their corresponding strengths a and sizes r are $a_1 = 1$, $a_2 = 1$, $a_3 = -1$ and $r_1 = r_2 = r_3 = 1$. Note that the third amplitude is negative and therefore represents an antisplat. The results of our method can be seen in Fig. 9a.

Next, we superimpose two potential vortices onto this flow. The first vortex is generated with the position $\mathbf{p}_{v1} = [-3, 0.5, 0]$ a strength of $a_{v1} = -1$ and a size $r_{v1} = 0.5$, whereas the second vortex has the position $\mathbf{p}_{v2} = [3, 0.5, 0]$ a strength of $a_{v1} = 1$ and the size $r_{v1} = 0.5$. This superposition is done for validation only. The resulting flow field does no more fulfill the non-penetration condition at the surface $y = 0$. (This could be accomplished, if desired, by adding mirrored vortices at the same distance below the surface, i.e., with their core at $y < 0$.) Fig. 9b shows the splat detection applied to the resulting velocity field. In addition to our
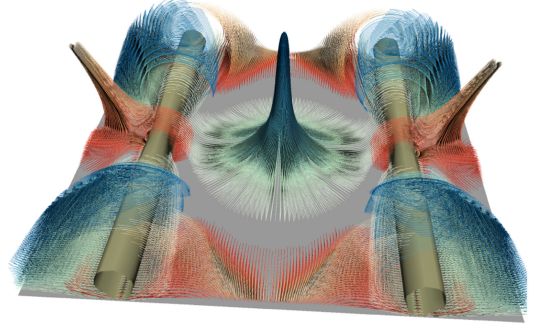
visualization scheme, we added an iso-contour of the λ_2-criterion [37] to highlight the vortices. The results were obtained with an offset distance of $\epsilon = 0.2$, a maximum integration time of $\tau = 2$ and a sample length of $\Delta_t = 0.1$.

Comparing the two images in Fig. 9 we infer a significant impact of the vortices on the flow field. Splats and antisplats emerge near the vortices, implying that the vortices splat fluid volume towards the boundary, also dragging it from the surface at other points. This suggests that our method detects splats and antisplats generated by a vortical flow pattern. A similar phenomenon is described by Rashidi [13] for a physically realistic configuration.

The flow field is further illustrated in Fig. 10 using our visualization scheme. Note that our method detects the bulk flow towards the surface being separated by the vortex as two individual splat events, as intended. The pathline visualization shows, that these individual phenomena originate from the same bulk flow. These results demonstrate that the proposed method reliably identifies the desired features, splats and antisplats, even if these are heavily modified by the surrounding flow.
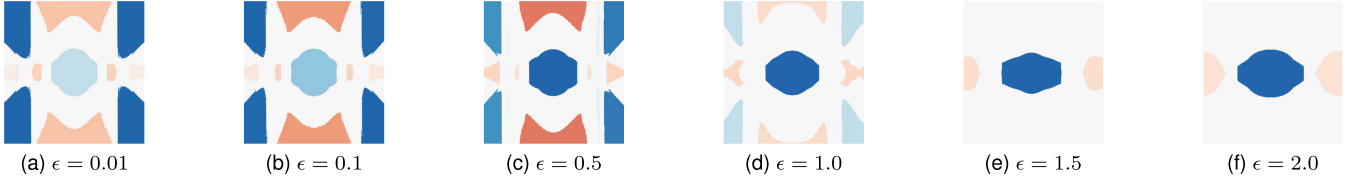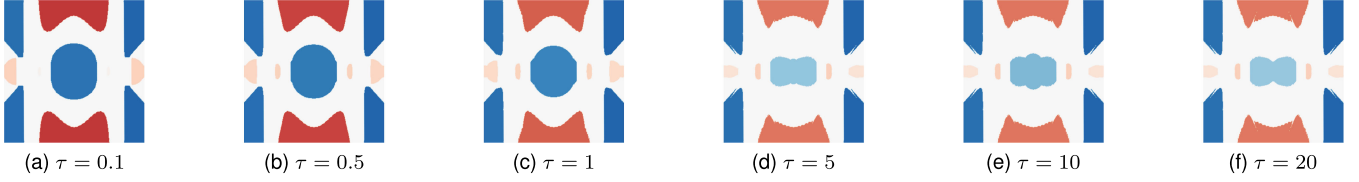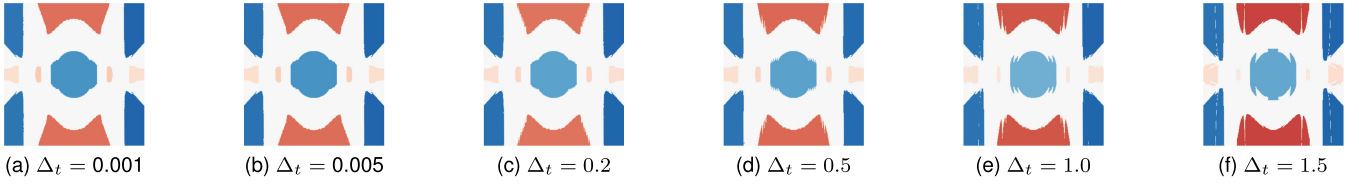
7 PARAMETERS AND PERFORMANCE

Various parameters are used in the new method, the offset distance ϵ, the maximum integration length τ, the sample length Δ_t. In this section, we study the influence of the individual parameters and derive a suitable strategy for their choice. Then, we examine the performance and scalability of our method by increasing the grid resolution. We base this study on an artificial dataset including multiple vortices, splats and antisplats. Splats, antisplats and vortices as well as the domain are generated according to Section 6.4.

7.1 Parameters

The reference set of parameter values for our analysis is $\epsilon = 0.2$, $\tau = 2$, $\Delta_t = 0.1$.

Offset Distance ϵ. The global offset distance is an influential parameter, as its choice directly affects the detected regions. Using a large offset distance the method is insensitive to small scaled flow features located between the offset plane and the flow boundary. In addition, the evaluation of Equation (13) may fail, as the flow pattern may change with increasing distance from the surface. Fig. 11 shows how a

(a) $\epsilon = 0.01$ (b) $\epsilon = 0.1$ (c) $\epsilon = 0.5$ (d) $\epsilon = 1.0$ (e) $\epsilon = 1.5$ (f) $\epsilon = 2.0$

Fig. 11. Sensitivity of the results to the offset distance ϵ for $\tau = 2$ and $\Delta_t = 0.1$.

(a) $\tau = 0.1$ (b) $\tau = 0.5$ (c) $\tau = 1$ (d) $\tau = 5$ (e) $\tau = 10$ (f) $\tau = 20$

Fig. 12. Sensitivity of the results to the integration time τ for $\epsilon = 0.2$ and $\Delta_t = 0.1$.

(a) $\Delta_t = 0.001$ (b) $\Delta_t = 0.005$ (c) $\Delta_t = 0.2$ (d) $\Delta_t = 0.5$ (e) $\Delta_t = 1.0$ (f) $\Delta_t = 1.5$

Fig. 13. Sensitivity of the results to the sampling distance Δ_t for $\epsilon = 0.2$ and $\tau = 2$.

large offset distance leads to an exclusion of the vortices in the resulting splat regions. Also, the relative splat/antisplat intensity visualized is shown to be highly sensitive. Therefore, ϵ should be chosen as small as possible to ensure the consistent detection of splat and antisplat events of all scales. Taking into account a flow with a no-slip boundary condition, this approach may be limited, as the velocity tends to zero with smaller and smaller wall distance. The choice of the offset distance, therefore, depends on the flow and in particular the Reynolds number, the spatial resolution of the data, and the boundary condition applied. In a turbulence-resolving simulation the grid resolution determines the finest turbulent scales being resolved. Hence, it is natural to relate the globally defined offset ϵ to the highest resolving cell size of the data analyzed. In the cases investigated we found that 6 to 7 cell layers away from the relevant surface to be a suitable offset distance.

Maximum Integration Time τ. The maximum integration time determines the structure of the splat regions detected. In the present analytical and steady cases, a very large integration time results in an increasing difference of the maximum times in which particles are advected due to the termination criterion. This behavior is generated by trajectories seeded in neighborhoods of B^ϵ converging toward the boundary surface, whereas those seeded outside these neighborhoods are terminated early. However, as our method is designed to capture splats in real-world simulations of turbulent flows, strict monotonicity of trajectories is not expected. Nonetheless, we recommend limiting the integration time to a reasonable value to avoid potential deformations and artifacts in the found splats due to this behavior. Using a very short integration time is not recommended as the resulting Cauchy-Green tensor represents an instantaneous analysis of the vector field on the boundary

surface for $\tau \to 0$. The impact of the termination criterion used for the integration is shown in Fig. 14. It shows a histogram of the maximal advection time of particles originating in the seeding points demonstrating that only few trajectories exhibit an excessive increase of the maximum integration time. We assume the large differences of maximum integration times to cause the deformations seen in Fig. 12. Note that in turbulent flows the flow direction exhibits strong fluctuations. This leads to a stronger impact of the abort criterion thus avoiding unreasonably long trajectories. Therefore we assume that our method is fairly robust to a long integration times.

As a heuristic for a suitable integration time, we recommend taking the offset distance and the instantaneous velocity field into account. An appropriate estimation is the integration time a massless particle needs to advect from the offset surface to the boundary surface. The instantaneous velocity field in normal direction at the offset boundary surface gives an idea of the scale in which particles advect near the boundary (in normal direction). We, therefore, utilize the offset distance divided by the mean (absolute) normal velocity at the discrete offset surface to provide the following rule of thumb for an appropriate integration time.

$$\tau = \epsilon \left[|B^\epsilon|^{-1} \sum_{\mathbf{x} \in B^\epsilon} |\langle \mathbf{v}(\mathbf{x}, t_0), \mathbf{n} \rangle| \right]^{-1}. \tag{18}$$

Sample Length Δ_t. The sample length determines the frequency in which the trajectories are sampled for the convolutions of the gradients. Therefore, a reasonably small value is desired, as high values lead to sampling artifacts, as seen in Fig. 13. With small scale turbulence and the resulting curved trajectories, a short sample length is required to fully
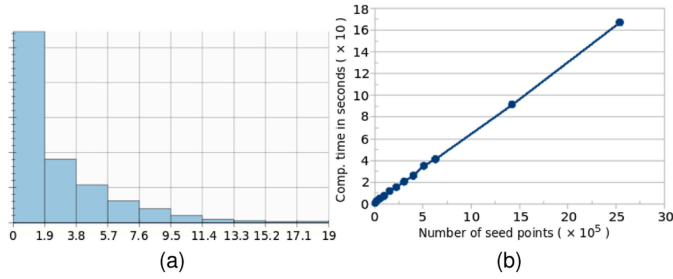
Fig. 14. Quantitative measures relative to the computed particle trajectories. (a) Histogram of the maximum advection times for the corresponding seed points. (b) Computation time in seconds required for the computation of the projected Cauchy-Green tensor plotted against the number of seed points.

capture the trajectories. We recommend selecting the sample length based on the grid resolution and the maximum velocity of the dataset. The idea is to estimate the time a particle with maximum velocity needs to pass through a single cell using the shortest path. Dividing this time by two guarantees at least one sample inside the cell. This leads to following rule of thumb for structured grids:

$$\Delta_t = \frac{1}{2} \frac{\min\{\Delta_x; \Delta_y; \Delta_z\}}{\max\|\mathbf{v}(\mathbf{x}, t)\|}, \qquad (19)$$

with the step sizes of the grid $\Delta_x, \Delta_y, \Delta_z$. Note that Δ_t is a constant parameter and the step sizes refer to the smallest cell of the grid. Our experience shows that minor changes to the obtained sample length do not alter the results significantly (cf. Fig. 13a and 13b).

7.2 Performance

In this section, we use the flow field to analyze the computational efficiency of our technique. The detection of the splat and antisplat events based on the resulting projected Cauchy-Green tensor employs a segmentation approach using a union find structure and the computation of singular points. For the computation of the singular points, we solve the linear systems of equations of the velocities at the vertices for each triangle utilizing linear interpolation. These steps have a time complexity of $\mathcal{O}(n)$.

We measured the computation time for the localized Cauchy-Green tensor based on the flow field generated in Section 6.4 for different grid resolutions. The parameter values are $\Delta_t = 0.01$, $\epsilon = 0.2$, $\tau = 2$ and a threefold subdivision was employed. Due to the autonomy of individual trajectories, the integration and computation is run parallelized using OpenMP. For the numerical integration we employed the Dormand-Prince method [38].

The tests where run on a Linux system with Ubuntu 16.04.1 LTS, 32 GB of RAM, and 32x Intel(R) Xeon(R) CPU E5-2630 v3 @ 2,40 GHz (hyperthreaded). As the runtime depends on the resolution of the offset boundary condition, we ran our measures all on the same domain using $n \times 40 \times n$ grid points, with n increased in intervals of 10 up to $n = 100$, starting at $n = 10$, and two additional samples, $n = 150$ and $n = 200$. The number of vertices used for seeding the trajectories is then plotted against the runtime in seconds (cf. Fig. 14). The method scales linearly with a computation time of approximately 3 minutes for an offset
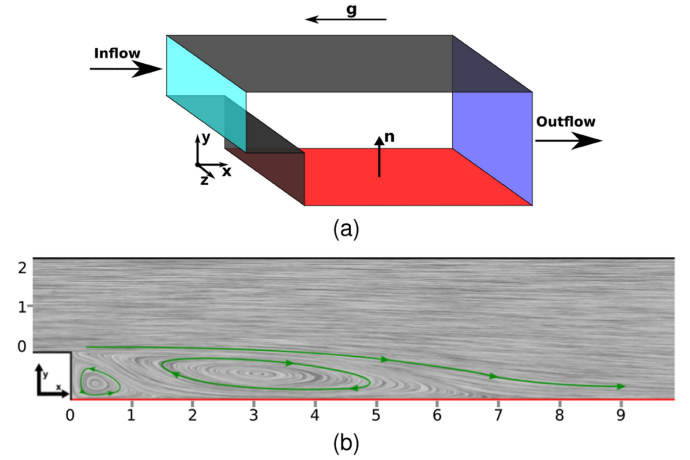

Fig. 15. Configuration and mean flow for the application case. (a) Sketch of the domain for the BFS flow simulation (not to scale). The surface of main interest is displayed in red. (b) Average flow of the presented simulation results visualized by *Line Integral Convolution*. The picture shows a zoom of the recirculation zone. Note that the domains shown in (a) and (b) are rotated clockwise by 90 degree. Visualizations in this paper are based on the rotated domain.

boundary surface containing approximately 2.5×10^6 control points. This is a fairly short computation time allowing for an application on large datasets and a convenient exploration of the parameter space.

Note that an increase of the maximum integration time τ and a decrease of the sample length Δ_t increase the computation time linearly.

8 BACKWARD-FACING STEP FLOW

In this section we apply our method to real world data. These were obtained by a so-called Direct Numerical Simulation (DNS), a simulation where the entire three-dimensional unsteady turbulent eddy motion was computed on a fine grid with a small time step. The configuration addressed here is the flow over a backward-facing step which is a frequently studied prototypical flow with separation, reattachment and recirculation. In fluid dynamics literature, this configuration has not yet been studied concerning splats and antisplats. In the following, data from a simulation conducted by Niemann and Fröhlich [39] are used, obtained for the configuration sketched in Fig. 15a with the step height h used as reference length throughout. The configuration features an expansion ratio of 1.5 with fully developed turbulent channel flow obtained from a separate precursor simulation injected at the upstream end. At the outlet, a so-called
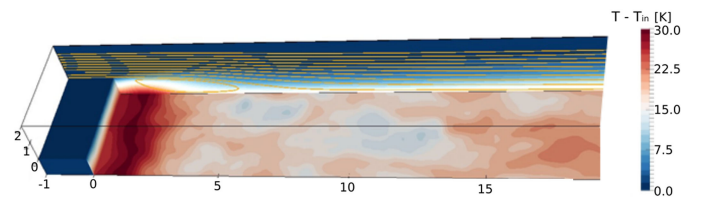

Fig. 16. Perspective view of the instantaneous wall temperature in the BFS flow obtained with a constant heat flux imposed on the streamwise wall behind the step. Gravity forces set to zero. The instant in time depicted here is not the same as for the flow field below. The streamlines (yellow) of the mean flow are depicted on the back vertical wall. They resemble the flow pattern shown in Fig. 15b.
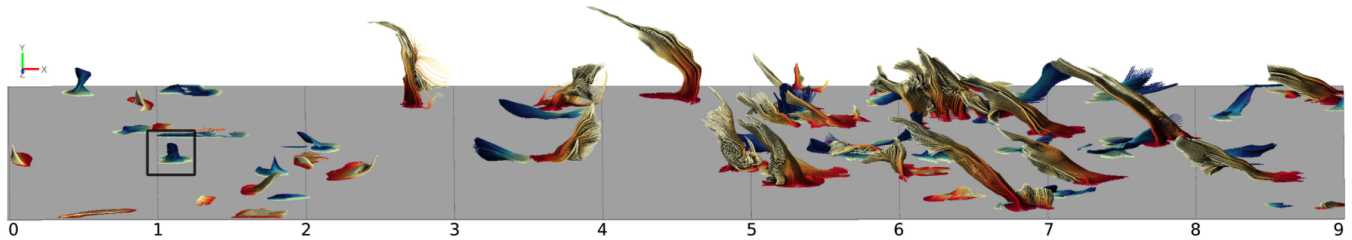
Fig. 17. Three-dimensional visualization of the detected splat regions. This figure shows the pathline visualization of the splat and antisplat regions shown in Fig. 18 for time step $t = 182.455$. The highlighted antisplat is shown in Fig. 20a.

convective outflow condition was applied and periodic conditions were imposed in spanwise direction. A no-slip condition was prescribed at all solid walls. The Reynolds number, built with the step height and the bulk velocity at the inlet was $Re = 4805$. The fluid considered was liquid metal with a Prandtl number of $Pr = 0.0088$. The wall behind the step (red wall in Fig. 15a was heated). The flow was directed upwards (see arrow for gravity in Fig. 15a), but in the particular simulation considered here the buoyancy term was turned off, which is realistic for very small temperature differences. The only influence of the temperature field then is a modification of the viscosity. With the temperature difference prevailing in this case this variation was very small so that the issue can be entirely disregarded for the present purpose.

To motivate the application of our method for splat and antisplat detection Fig. 16 shows the wall temperature at an arbitrary instant in time. Since the heat flux is imposed the wall temperature depends on the amount of cooling provided by the flow. Obviously, the instantaneous wall temperature varies exhibiting regions of lower values which are related to locally impinging colder fluid. Note that the temperature field must be substantially smoother than the velocity field in this flow due to the high thermal conductivity of the liquid metal simulated, i.e., due to the very low Prandtl number of this fluid.

The mean flow of the BFS configuration is shown in Fig. 15b. It features a curved shear layer between the outer flow and a recirculation region behind the step. Reattachment in the mean flow occurs at $x_r = 7h$. Inside the recirculation zone, a secondary vortex is observed right behind the step inducing separation of the mean backflow flow near the wall around $x_s = 1.9h$.

Physical issues of the complex turbulent flow in this comparatively simple setup are discussed in numerous papers. Simpson [40] provides an introduction to this topic and stresses that the instantaneous separation and reattachment lines are highly unsteady and can deviate substantially from the mean by as much as $\pm 2h$. Further, and more recent references are given in [39]. In the present study, the goal is to illustrate the kind of results which can be obtained with our method, rather than to delve into a detailed discussion of the physics, so that we remain short on the latter.

The DNS of [39] was conducted using a Cartesian grid with $662 \times 292 \times 192$ points to cover the computational domain of extent $[-2; 20] \times [-1; 2] \times [0; 4]$ in streamwise, wall-normal and spanwise direction, respectively, with grid lines also covering the volume underneath the step and clustered near solid walls, as described in the cited reference. Note that the dataset excludes the top and bottom cell layers as these are trivial due to the no-slip boundary condition ($u = v = 0$). As a result, the lower bound for the field data used here is $y_{min} = -0.998844$. Data on the highly resolving DNS grid were obtained with a time step 0.05 during the simulation which is excessively small and due to stability restrictions of the DNS code. Hence, for the present study the interval $[180.056; 184.855]$ was selected and seven fields with a constant time interval of 0.8 used to evaluate our method. The analysis focuses on the wall behind the step (red plane in Fig. 15b, wall normal vector $\mathbf{n} = [0; 1; 0]$) up to $x = 9$ and the near-wall region close to it. The trajectories for the computation were seeded at time step $t = 182.455$.

We compute the offset surface with a distance of $\epsilon = 0.013844$ from the wall and apply the subdivision threefold. This results in a simplicial offset grid with approximately 5.7×10^6 control points.

For our splat detection we apply a maximum integration length of $\tau = 2.4$ and a sample length of $\Delta_t = 0.01$. The com-
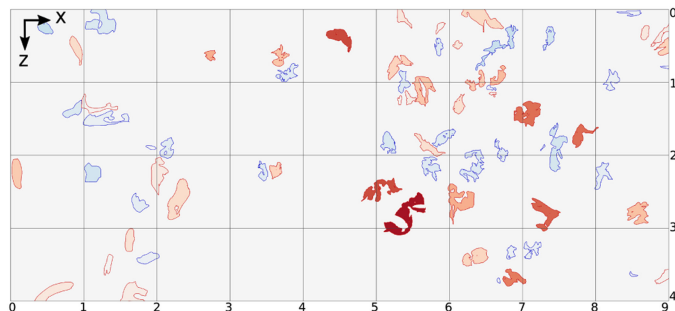

Fig. 18. Splat and antisplat regions detected on the offset surface within the backward-facing step flow. This image shows the splat visualization of the recirculation region behind the step ($x = 0$). These were generated for the time step $t = 182.455$
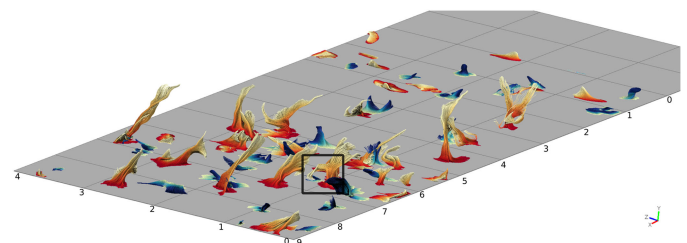

Fig. 19. Three-dimensional visualization of the detected splat regions. This figure is analogous to Fig. 17 with a perspective chosen for a better overview. The highlighted phenomenon is shown in Fig. 20b
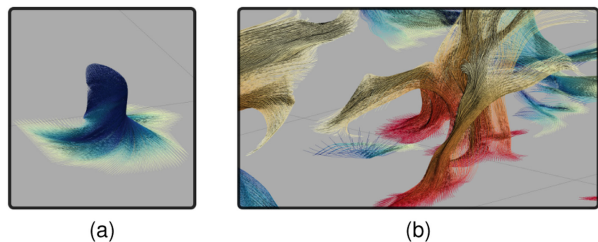
Fig. 20. Detailed visualizations. (a) Fully developed isolated antisplat extracted from Fig. 17. (b) Splat seen in Fig. 19 with a flow pattern suggesting the presence of a vortical structure.
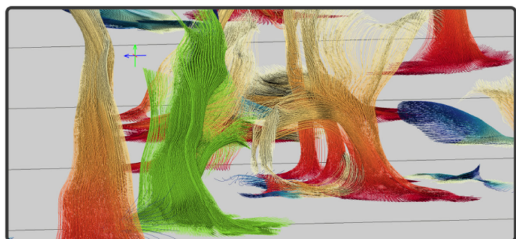

Fig. 21. An example for splat highlighting within the region shown in Fig. 20b. The highlighted splat (green) corresponds to the splat region located at $[x; z] \approx [7; 1.4]$ on the offset surface (see. Fig. 18).

putation of splat and antisplat regions with this configuration took approximately 10 minutes.

The results are shown in the Figs. 17, 18, 19. Our visualization of the splat regions shown in Fig. 18 allows for a clear evaluation of the relative splat strengths. The detected regions also show that our method detects splat and antisplat phenomena of various scales and strengths. Even strongly deformed splat/antisplat regions are reliably detected. The corresponding pathline visualizations shown in Figs. 17, 20, and 19 suggest that the detected events are splats and antisplats, indeed.

It is apparent that particularly strong splat events occur in the region $x \approx 5 \dots 8$ where the mean flow reattaches (cf. Fig. 15b). Also, Fig. 17 illustrates that the splats arrive in an oblique way with the mean flow, but are detected nevertheless. Also, antisplats are observed there, presumably due to continuity and induced by other vortical structures (cf. Fig. 19). A second region of increased (anti)splat activity is seen for $x \approx 1 \dots 2$. It is related to the mean upward motion at the rear end of the secondary vortex in the corner. One case is highlighted in Fig. 20a. Fig. 18 shows that these are much weaker than those in the reattachment area. The isolated antisplats are highlighted in Fig. 20 and often rotate. The antisplats seem to form along a vortex line – or generate this line themselves. This is an issue requiring further physical analysis which is beyond the present scope and will be the subject of future domain investigations. The immediate observations made here are new for the field and so far have not been discussed in the literature on this configuration. This, again, demonstrates the usefulness of the present tool for fluid mechanics research.

9   CONCLUSIONS AND FUTURE WORK

In this paper, we developed a Lagrangian method for the identification of splat and antisplat events in turbulent flow

fields. With the new method, these can be detected reliably, regardless of scale and strength of impact. We evaluated the method utilizing a small, self-written splat generation tool and applied the proposed detection scheme to various synthesized flow fields generated with this tool containing splats and antisplats. We have shown that splats and antisplats can be extracted reliably even in a fairly complex situation. This setting was then used to assess the influence of algorithmic parameters which allowed us to propose suitable values for a robust extraction of splats and antisplats. Another contribution is a suitable three-dimensional visualization scheme for the detected splats and antisplats by rendering pathlines involved in these events, with emphasis on spatial and structural perception. Furthermore, a two-dimensional visualization scheme on the boundary surface was provided allowing an intuitive assessment of the size, strength, and distribution of splat/antisplat events. The method was then employed for a real-world application case, DNS data of a BFS flow. The results reported highlight the capabilities of the new method in coping with highly complex turbulent velocity fluctuations of a fully turbulent flow field. It is evident that the proposed method is ready for application to a vast range of near-wall flows now. The fluid mechanicists among the authors of this paper found the method extremely helpful as it is able to extract a type of coherent flow structures to permit investigations about their role in a complex turbulent flow near a boundary. New DNS data for free surface flows with aquatic canopies, for example, are being generated in the group of the third author [41] and will undergo examinations with the tool presented here.

The proposed method opens a variety of perspectives. Underway is the extension by the present authors to arbitrary smooth boundaries and an application to turbomachinery flows. Another target is the investigation of splats and antisplats over time, thus providing information about their emergence, propagation, and dissipation, for example. Furthermore, the new scheme can be used to quantify the impact of splats and antisplats on the momentum budget of near-wall turbulent flow fields and their impact on transfer processes, such as heat transfer. Studying these effects with the help of the proposed scheme can enhance the physical understanding of turbulent near-wall flows and aid in the development of statistical models in separation and reattachment regions.

REFERENCES

[1]   B. Perot and P. Moin, "Shear-free turbulent boundary layers. part 1. physical insights into near-wall turbulence," *J. Fluid Mech.*, vol. 295, pp. 199–227, Jul. 1995.
[2]   J. Magnaudet, "High-reynolds-number turbulence in a shear-free boundary layer: Revisiting the HuntGraham theory," *J. Fluid Mech.*, vol. 484, pp. 167–196, Jun. 2003.

[3] J. C. Hunt and J. F. Morrison, "Eddy structure in turbulent boundary layers," *Eur. J. Mech. - B/Fluids*, vol. 19, no. 5, pp. 673–694, Sep. 2000.

[4] K. Nagata, J. C. R. Hunt, Y. Sakai, and H. Wong, "Distorted turbulence and secondary flow near right-angled plates," *J. Fluid Mech.*, vol. 668, pp. 446–479, Dec. 2010.

[5] W.-T. Tsai, "A numerical study of the evolution and structure of a turbulent shear layer under a free surface," *J. Fluid Mech.*, vol. 354, pp. 239–276, Jan. 1998.

[6] L. Shen, X. Zhang, D. K. P. Yue, and G. S. Triantafyllou, "The surface layer for free-surface turbulent flows," *J. Fluid Mech.*, vol. 386, pp. 167–212, May 1999.

[7] W.-T. Tsai, S.-M. Chen, and C.-H. Moeng, "A numerical study on the evolution and structure of a stress-driven free-surface turbulent shear flow," *J. Fluid Mech.*, vol. 545, no. 1, Dec. 2005, Art. no. 163.

[8] Y. Pan and S. Banerjee, "A numerical study of free-surface turbulence in channel flow," *Phys. Fluids*, vol. 7, no. 7, pp. 1649–1664, Jul. 1995.

[9] P. Bradshaw, "A note on poisson's equation for pressure in a turbulent flow," *Phys. Fluids*, vol. 24, no. 4, 1981, Art. no. 777.

[10] J. Bodart, J. B. Cazalbou, and L. Joly, "Direct numerical simulation of unsheared turbulence diffusing towards a free-slip or no-slip surface," *J. Turbulence*, vol. 11, Jan. 2010, Art. no. N84.

[11] R. Nagaosa, "Direct numerical simulation of vortex structures and turbulent scalar transfer across a free surface in a fully developed turbulence," *Phys. Fluids*, vol. 11, no. 6, pp. 1581–1595, Jun. 1999.

[12] J. R. Taylor, S. Sarkar, and V. Armenio, "Large eddy simulation of stably stratified open channel flow," *Phys. Fluids*, vol. 17, no. 11, Nov. 2005, Art. no. 116602.

[13] M. Rashidi, "Burst–interface interactions in free surface turbulent flows," *Phys. Fluids*, vol. 9, no. 11, pp. 3485–3501, Nov. 1997.

[14] A. Dejoan and M. A. Leschziner, "Separating the effects of wall blocking and near-wall shear in the interaction between the wall and the free shear layer in a wall jet," *Phys. Fluids*, vol. 18, no. 6, 2006, Art. no. 065110.

[15] J. Fröhlich, C. P. Mellen, W. Rodi, L. Temmerman, and M. A. Leschziner, "Highly resolved large-eddy simulation of separated flow in a channel with streamwise periodic constrictions," *J. Fluid Mech.*, vol. 526, pp. 19–66, Mar. 2005.

[16] V. DeAngelis, P. Lombardi, and S. Banerjee, "Direct numerical simulation of turbulent flow over a wavy wall," *Phys. Fluids*, vol. 9, no. 8, pp. 2429–2442, Aug. 1997.

[17] A. Keating, U. Piomelli, K. Bremhorst, and S. Nesic, "Large-eddy simulation of heat transfer downstream of a backward-facing step," *J. Turbulence*, vol. 5, pp. 20–1–27, May 2004.

[18] L. Wang, Y.-H. Dong, and X.-Y. Lu, "Large eddy simulation of turbulent open channel flow with heat transfer at high prandtl numbers," *Acta Mech.*, vol. 170, no. 4, pp. 227–246, Jun. 2004.

[19] H. Hopf, "Vektorfelder in n-dimensionalen-mannigfaltigkeiten," *Mathematische Annalen*, vol. 96, pp. 225–250, 1927. [Online]. Available: http://eudml.org/doc/159166

[20] T. Salzbrunn and G. Scheuermann, "Streamline predicates," *IEEE Trans. Vis. Comput. Graph.*, vol. 12, no. 6, pp. 1601–1612, Nov. 2006. [Online]. Available: http://dx.doi.org/10.1109/TVCG.2006.104

[21] T. Salzbrunn, C. Garth, G. Scheuermann, and J. Meyer, "Pathline predicates and unsteady flow structures," *Visual Comput.*, vol. 24, no. 12, pp. 1039–1051, Dec. 2008. [Online]. Available: https://doi.org/10.1007/s00371-007-0204-x

[22] S. Dutta and H.-W. Shen, "Distribution driven extraction and tracking of features for time-varying data analysis," *IEEE Trans. Vis. Comput. Graph.*, vol. 22, no. 1, pp. 837–846, Jan. 2016.

[23] G. Haller, "Lagrangian coherent structures," *Annu. Rev. Fluid Mech.*, vol. 47, pp. 137–162, 2015.

[24] G. Froyland and K. Padberg, "Almost-invariant sets and invariant manifolds connecting probabilistic and geometric descriptions of coherent structures in flows," *Physica D: Nonlinear Phenomena*, vol. 238, no. 16, pp. 1507–1523, 2009.

[25] C. Garth, A. Wiebel, X. Tricoche, K. Joy, and G. Scheuermann, "Lagrangian visualization of flow-embedded surface structures," *Comput. Graph. Forum*, vol. 27, no. 3, pp. 1007–1014, 2008.

[26] F. Sadlo, A. Rigazzi, and R. Peikert, *Time-Dependent Visualization of Lagrangian Coherent Structures by Grid Advection*. Berlin, Germany: Springer, 2011, pp. 151–165.

[27] G. T. Chapman and L. A. Yates, "Topology of flow separation on three-dimensional bodies," *Appl. Mech. Rev.*, vol. 44, no. 7, pp. 329–345, Jul. 1991.

[28] G. Haller and G. Yuan, "Lagrangian coherent structures and mixing in two-dimensional turbulence," *Physica D: Nonlinear Phenomena*, vol. 147, no. 34, pp. 352–370, 2000.

[29] T. Hermann, "On the smoothness of offset surfaces," *Comput. Aided Geometric Des.*, vol. 15, no. 5, pp. 529–533, May 1998.

[30] J. Kasten, C. Petz, I. Hotz, B. R. Noack, and H.-C. Hege, "Localized finite-time lyapunov exponent for unsteady flow analysis," in *Proc. Vis. Model. Vis.*, 2009, pp. 265–274.

[31] G. A. Holzapfel, *Nonlinear Solid Mechanics: A Continuum Approach for Engineering*, vol. 1. Hoboken, NJ, USA: Wiley, Feb. 2000.

[32] K. Moreland, *Diverging Color Maps for Scientific Visualization*. Berlin, Germany: Springer, 2009, pp. 92–103.

[33] S. Eichelbaum, M. Hlawitschka, and G. Scheuermann, "Lineao–improved three-dimensional line rendering," *IEEE Trans. Vis. Comput. Graph.*, vol. 19, no. 3, pp. 433–445, Mar. 2013.

[34] P. Rheingans, "Task-based color scale design," in *Proc. Appl. Image Pattern Recognit.*, 1999, pp. 35–43.

[35] J. Spurk and N. Aksel, *Strömungslehre: Einführung in die Theorie der Strömungen; mit Aufgaben und Übungsbeispielen auf CD-ROM*, vol. 6. Berlin, Germany: Springer-Verlag, 2006.

[36] G. Kindlmann, "Superquadric tensor glyphs," in *Proc. 6th Joint Eurographics - IEEE TCVG Conf. Vis.*, 2004, pp. 147–154.

[37] J. Jeong and F. Hussain, "On the identification of a vortex," *J. Fluid Mech.*, vol. 285, pp. 69–94, 1995.

[38] J. Dormand and P. Prince, "A family of embedded runge-kutta formulae," *J. Comput. Appl. Math.*, vol. 6, no. 1, pp. 19–26, 1980. [Online]. Available: http://www.sciencedirect.com/science/article/pii/0771050X80900133

[39] M. Niemann and J. Fröhlich, "Buoyancy-affected backward-facing step flow with heat transfer at low Prandtl number," *Int. J. Heat Mass Transfer*, vol. 101, pp. 1237–1250, 2016.

[40] R. L. Simpson, "Turbulent boundary-layer separation," *Annu. Rev. Fluid Mech.*, vol. 21, pp. 205–234, 1989.

[41] S. Tschisgale, R. Meller, and J. Fröhlich, "Simulation of the turbulent flow over an array of flexible blades," in *Proc. 10th Int. Symp. Turbulence Shear Flow Phenomena*, 2017. [Online]. Available: http://www.tsfp-conference.org/proceedings/2017/2/230.pdf

Baldwin Nsonga received the BSc degree from the TU Bergakademie Freiberg, in 2013 and the MSc degree from the Leipzig University, in 2016. He is working towards the doctorate degree in the Institute of Computer Science, Image and Signal Processing Group, Leipzig University. His research interest includes flow visualization.

Martin Niemann received the doctorate degree from the Technische Universität Dresden where he investigated buoyancy-affected liquid metal flows and published several papers on this topic, in 2017. He is currently working as a consultant with DCS Computing. His research interests include turbulence, heat transfer, and particulate flows.

Jochen Fröhlich received the diploma degree in mechanical engineering from RWTH Aachen, Germany, in 1987 and the PhD degree in engineering science from Université de Nice - Sophia-Antipolis, France, in 1990. Since 2007 he is a full professor with TU Dresden. He has coauthored more than 200 reviewed book chapters, journal articles and conference papers, and has written a textbook on Large Eddy Simulation. His current research interests include numerical fluid mechanics, modeling and simulation of turbulent flows and multiphase flows. He is member of the editorial board of "Archive of Applied Mechanics" and organizes a biannual summer school on turbulence simulation.

Joachim Staib is working toward the PhD degree at the Technische Universität Dresden since 2014. His research interests include particle visualization and Focus+Context methods. He has authored numerous papers in the field of particle visualization.

Stefan Gumhold received the habilitation degree in computer science from the University of Tübingen. He is a professor in computer graphics and visualization with the TU Dresden in Germany. He has authored more than 80 papers in the areas computer graphics, visualization, and computer vision. His research interests include visual analysis, geometry processing and scene understanding. He is a member of the Eurographics Association.

Gerik Scheuermann received the master degree (diplom) in mathematics in 1995 and the PhD degree in computer science in 1999, both from the Technical University of Kaiserslautern. He is a full professor with the Leipzig University since 2004. He has coauthored more than 200 reviewed book chapters, journal articles, and conference papers. His current research interests include visualization and visual analytics, especially on feature and topology-based methods, flow visualization, tensor visualization, environmental visualization, document visualization and visualization for life sciences. He has served as paper cochair for Eurovis 2008, IEEE SciVis 2011, IEEE SciVis 2012, and IEEE PacificVis 2015. He has organized TopoInVis 2007, AGACSE 2008 and EuroVis 2013, as well as two Dagstuhl Seminars on Visualization. He is a member of the IEEE.

▷ **For more information on this or any other computing topic, please visit our Digital Library at** www.computer.org/csdl.